Supplementary Materials

Localized crack-enabled mechanical switching through micro-nano interfacial control of fracture pathways

Kibeom Kim[1,#], Sang Jin Park[1,#], Sangmin Oh[1], Myoung-Woon Moon[1,2,3,*], Hyesung Cho[1,*]

[1]Extreme Materials Research Center, Korea Institute of Science and Technology, Seoul 02792, Republic of Korea.
[2]School of Chemical Engineering, Sungkyunkwan University (SKKU), Suwon 16419, Republic of Korea.
[3]KIST-SKKU Carbon-Neutral Research Center, Sungkyunkwan University (SKKU), Suwon 16419, Republic of Korea.
[#]These authors contributed equally to this work.

[*]**Correspondence to:** Dr. Myoung-Woon Moon, Dr. Hyesung Cho, Extreme Materials Research Center, Korea Institute of Science and Technology, Seoul 02792, Republic of Korea. E-mail: mwmoon@kist.re.kr; hcho@kist.re.kr

Supplementary Video 1. Micro-notch fabrication via virtual-mask-guided UV curing. The video demonstrates the fabrication process of a soft substrate with a U-shaped microscale notch using a digital virtual mask and defocus-controlled UV projection in this study. The projected light pattern guided by the virtual mask and subsequent photocuring behavior during the UV-exposure process are visualized.

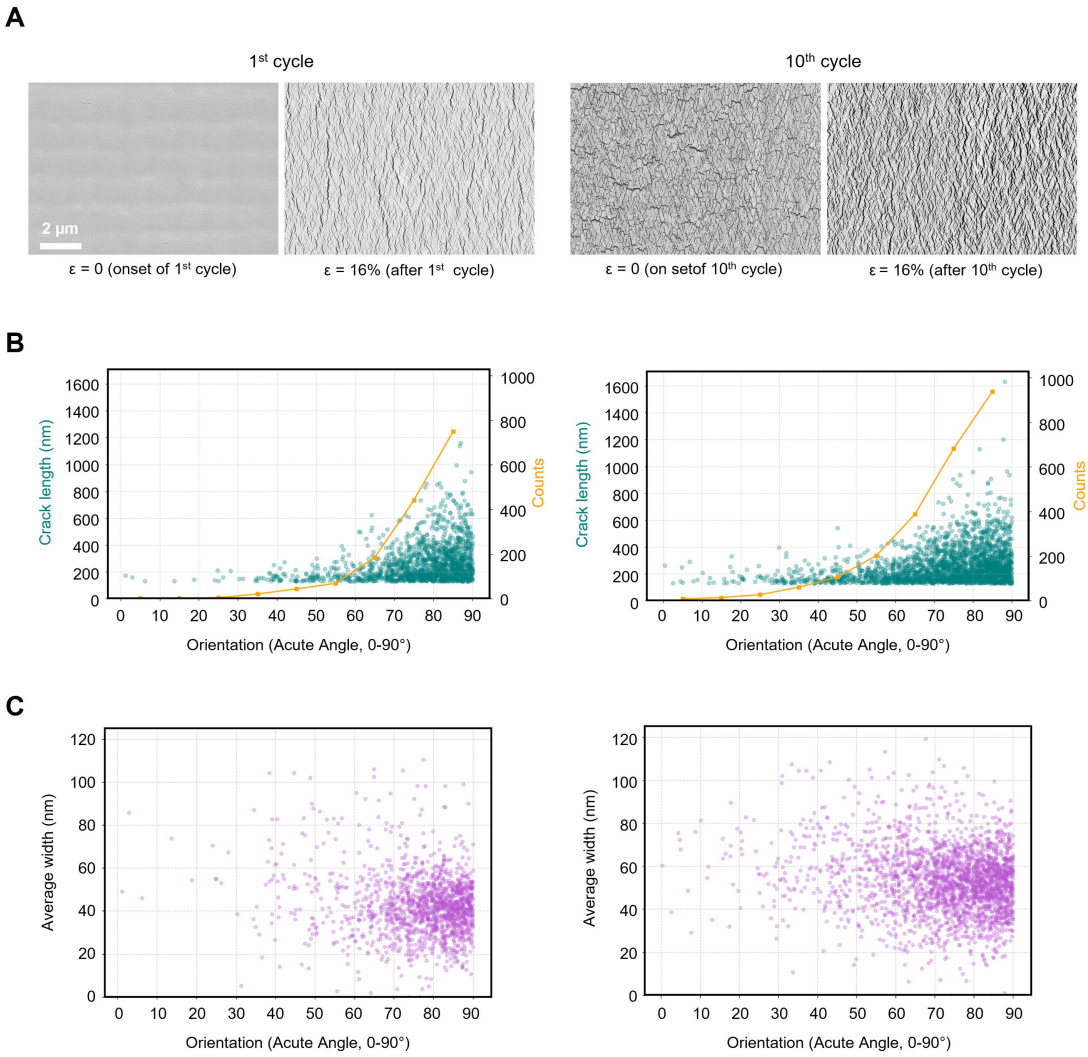

Supplementary Figure 1. Crack distribution in a metal thin film on a planar NOA substrate under tensile deformation. (A) Surface SEM images observed at ε=0 (beginning of each cycle) and ε=16% during the 1st and 10th loading cycles. Scale bar: 2μm.; (B) Individual crack length (teal scatter, left axis) and the number of cracks in each orientation interval (orange curve, light axis) plotted as a function of crack orientation (left: 1st cycle, right: 10th cycle). These plots are extracted from the SEM image in (A) using the ImageJ ridge detection plugin. Orientation is defined as the acute angle between the crack propagation direction and the tensile direction. With increasing tensile cycles, the number of cracks increases, and the orientation-dependent crack length follows a half-normal distribution. Note that the observed lower bound in crack length does not represent a physical minimum crack length, but reflects the image-processing detection threshold of 100 nm applied during Ridge Detection analysis.; (C) Scatter plot of the average crack width as a function of crack orientation (left: 1st cycle, right: 10th cycle). Cracks are predominantly distributed near orientations perpendicular to the tensile direction (~ 90°), and the average crack width increase with increasing cycle number.

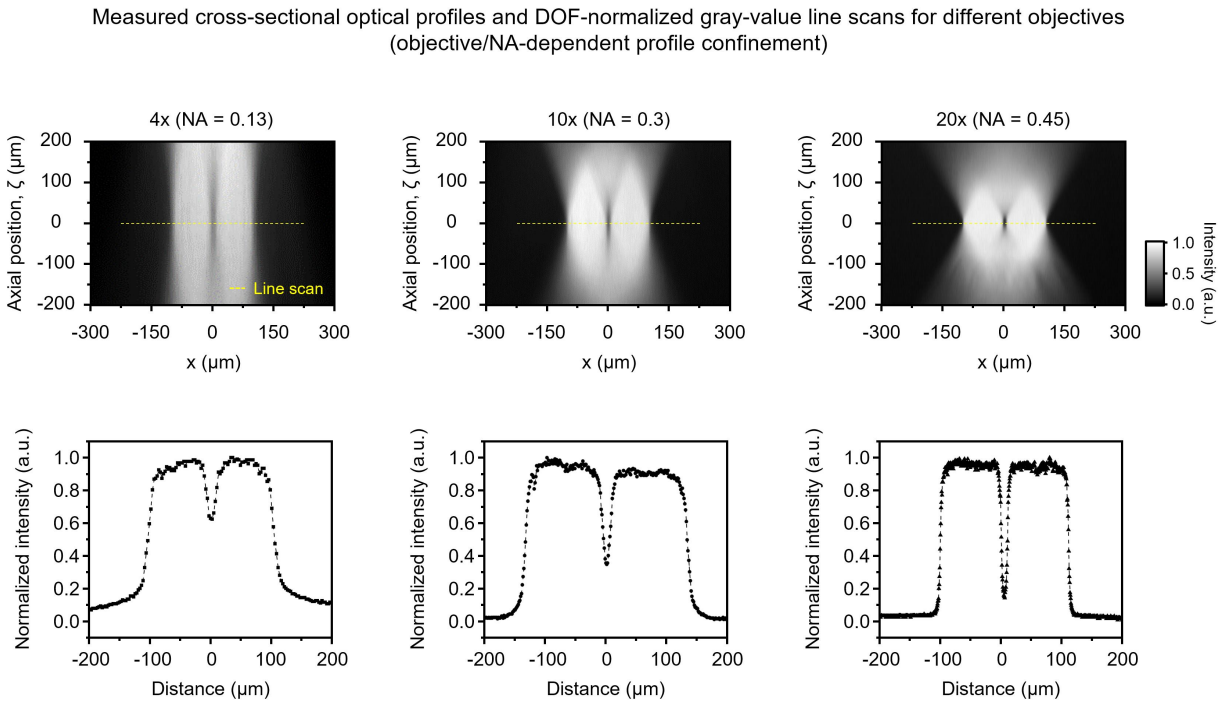

Supplementary Figure 2. Measured optical cross-sectional profiles and normalized gray-value line scans within the DOF region under different objective lens conditions (i.e., magnification/NA). (Top) Cross-sectional images of the measured optical intensity profiles for each objective lens condition. The yellow dashed lines indicate the positions where line scans were performed within the DOF region. The color bar on the right represents normalized intensity (gray value, a.u.).; (Bottom) Comparison of gray-value line profiles extracted along the yellow dashed lines in the top images, normalized with respect to the DOF reference. The results show that slit peak-gap contrast and profile sharpness vary depending on the objective lens condition, supporting the validity of the selected objective lens parameters used in this study.

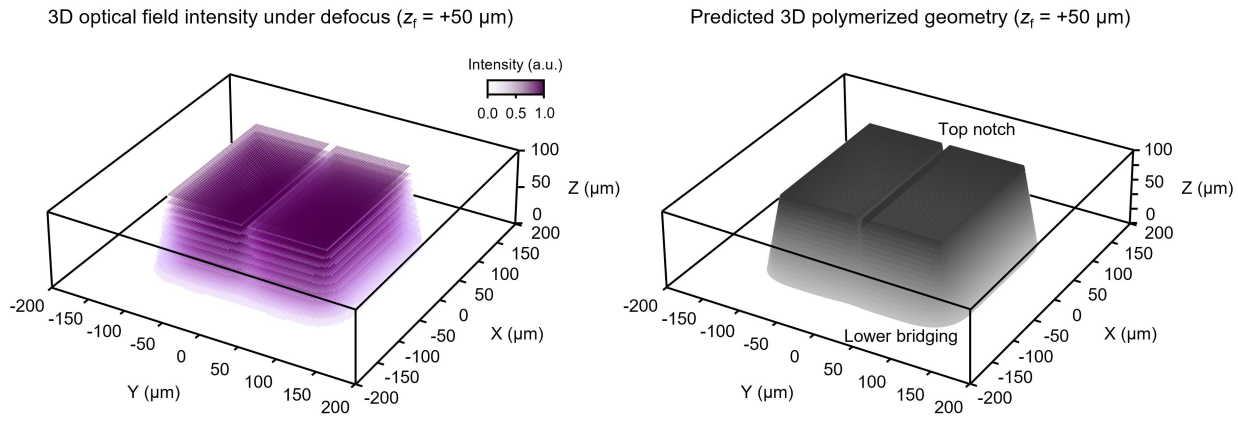

Supplementary Figure 3. Three-dimensional optical field distribution under defocus conditions and schematic prediction of the resulting 3D photocured structure. (Left) Schematic optical field simulation showing the cross-sectional slices at 10 μm intervals across a total thickness of 100 μm. The distribution visualizes the progressive diffusion and overlap of the two slit patterns along the depth (z) direction under defocus conditions.; (Right) Conceptual reconstruction of the predicted 3D structure based on the optical field distribution shown on the left. The model illustrates the formation of an asymmetric cross-section in which a top notch is preserved while lower bridging is formed in the bottom region.

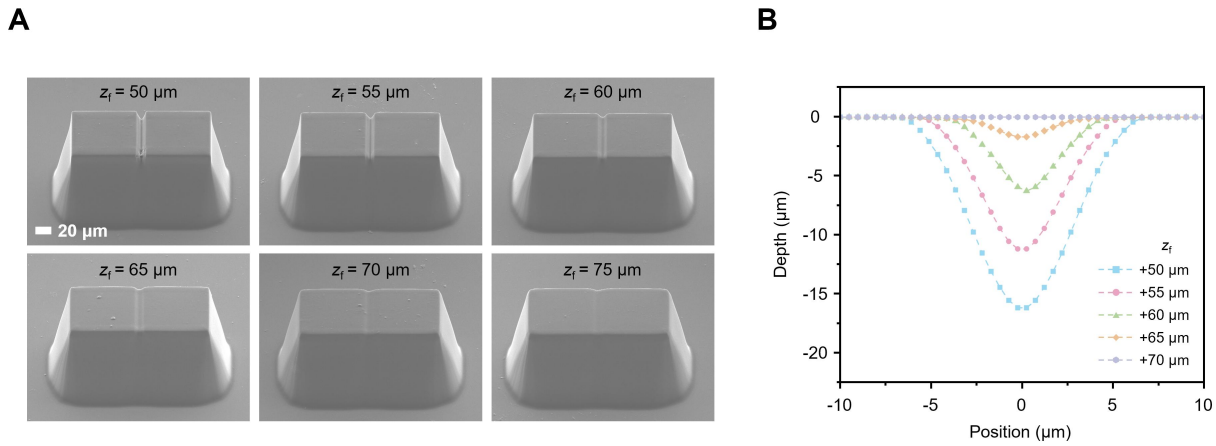

Supplementary Figure 4. Experimental-simulation comparison of notch geometry as a function of focal position (z_f). (A) SEM images of photocured structures fabricated under different focal positions. The results show stepwise modulation of the top-notch geometry and depth with increasing z_f.; (B) Simulated notch profiles calculated under various z_f conditions. The simulation results exhibit consistent trends in the relative notch depth variation in the experimental data.

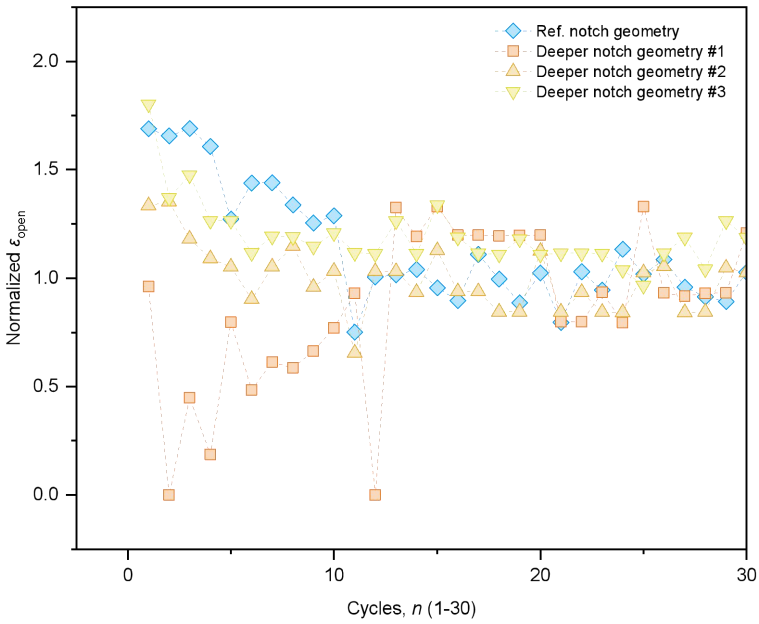

Supplementary Figure 5. Robustness of the switching threshold under notch-depth variation. The Reference specimen denotes the Cond. 4 device with the notch geometry used in Figure 4D of the main manuscript. The Deeper-notch #1–#3 specimens were fabricated under the same Cond. 4 processing conditions but with intentionally deeper U-shaped notches than the Reference. The cycle-by-cycle ε_{open} values were normalized by the mean ε_{open} of each specimen, so that switching-threshold stability could be compared independently of differences in absolute threshold strain. The normalized ε_{open} values show that the switching response is maintained during repeated cycling not only for the Reference geometry but also for the deeper-notch specimens, supporting that the proposed mechanical switching behavior can be maintained within a practical notch-depth working regime.

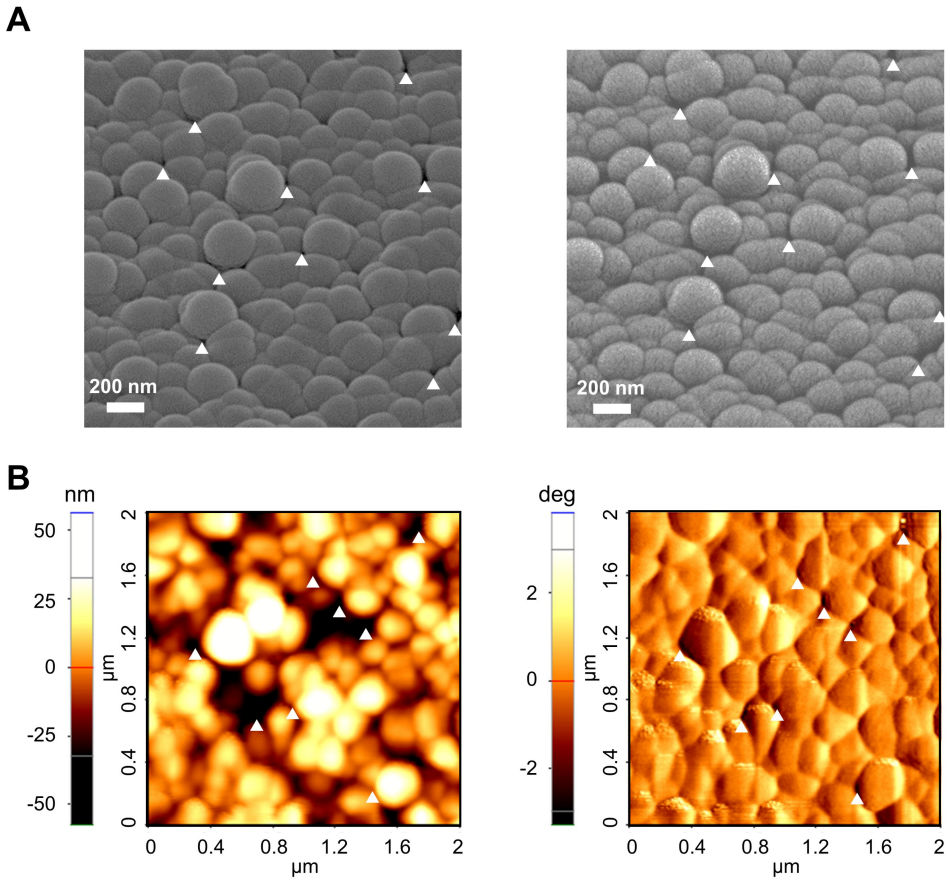

Supplementary Figure 6. Microstructural characterization of the HMDSO/Pt bilayer deposited on plasma-induced nanostructures, confirming conformal coverage and the integrity of the percolation network. (A) Top-view SEM images of the HMDSO/Pt-coated nanostructured surface. Left: secondary-electron (SE) image, emphasizing the surface topography of the conformal bilayer. Right: backscattered-electron (BSE) image of the same region, providing compositional and topographic contrast. White triangular markers indicate representative nanoscale pores formed during deposition; within the 2×2 μm² field of view, fewer than ten such pores are observed, with lateral dimensions ranging from a few to several tens of nanometers.; (B) Atomic force microscopy (AFM) characterization of the same surface. Left: topography (height) image showing the conformal envelope of the underlying nanostructure (height range: −50 to +50 nm). Right: phase image of the same area (range: −3 to +3°). Dark regions in the topography image correspond to a continuous, uniform phase signal, confirming that the Pt overlayer remains electrically connected across topographic depressions and that the percolation network is intact without macroscopic discontinuities.

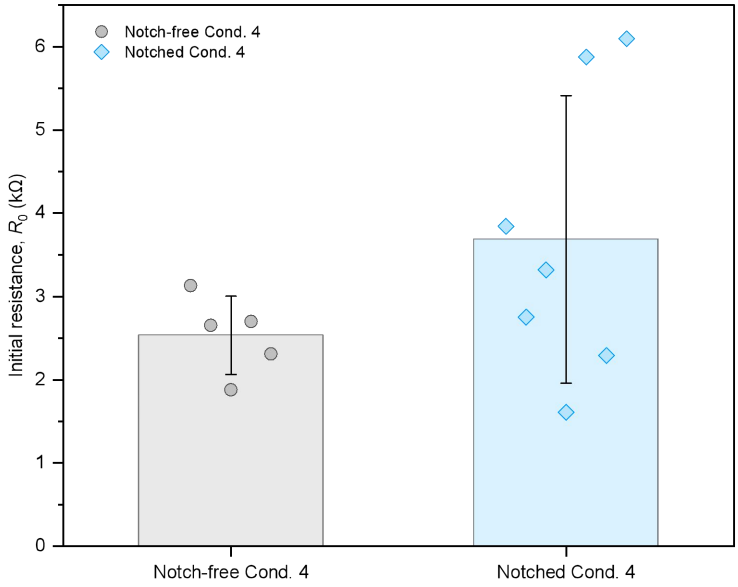

Supplementary Figure 7. Multi-device statistics of the initial resistance (R_0) measured prior to preconditioning for the Notch-free Cond. 4 and Notched Cond. 4 conditions. Each resistance value was measured immediately after mounting the specimen on the tensile stage, before the initial preconditioning cycle. The Notched Cond. 4 specimens, fabricated under the 55 mTorr sputtering condition (n = 7), exhibited a mean initial resistance of 3.68 ± 1.73 kΩ. The Notch-free Cond. 4 control, fabricated under the identical process condition but without the U-shaped notch (n = 5), exhibited a mean initial resistance of 2.53 ± 0.47 kΩ. Both conditions lie within the kΩ-level range. The larger variability in the Notched Cond. 4 (CV ≈ 47%, versus ≈ 19% for the notch-free control) is consistent with the localized geometric bottleneck introduced by the notch rather than with process-level instability of the Pt deposition.

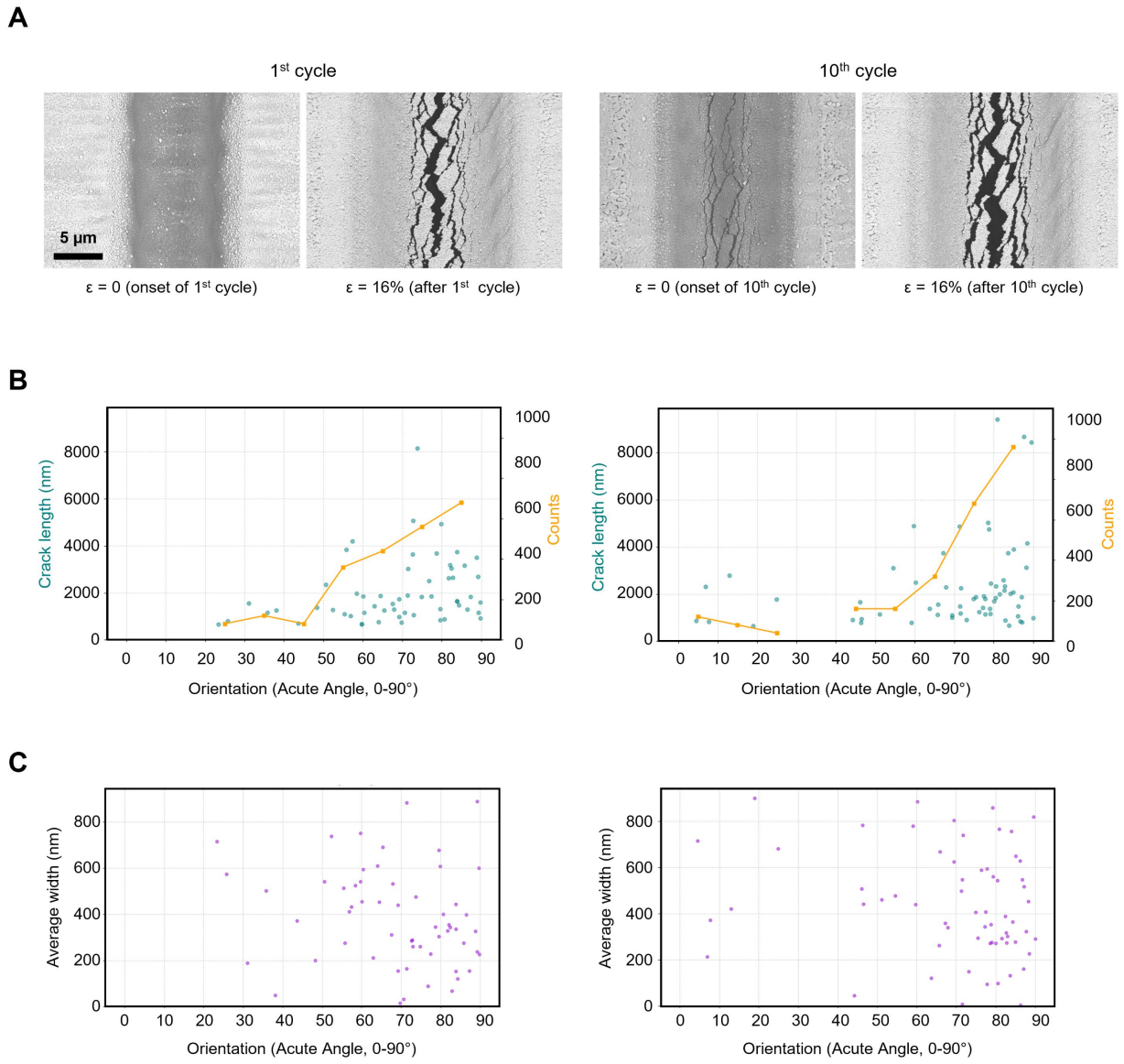

Supplementary Figure 8. Crack distribution in a metal thin film deposited on a micro-notch/nanostructures/HMDSO layer under tensile deformation. (A) Surface SEM images observed at ε=0 (beginning of each cycle) and ε=16% during the 1st and 10th loading cycles. Even after 10 cycles, the cracks exhibit good morphological conformity upon reclosure. Compared to the planar NOA substrate, a smaller number of cracks with longer crack lengths are observed.; (B) Individual crack length (teal scatter, left axis) and the number of cracks within each orientation interval (orange curve, right axis) plotted as a function of crack orientation (left: 1st cycle, right: 10th cycle).; (C) Scatter plot of average crack width as a function of crack orientation (left: 1st cycle, right: 10th cycle). Cracks are predominantly distributed near orientations perpendicular to the tensile direction, while a small number of cracks are additionally observed at lower orientation angles.

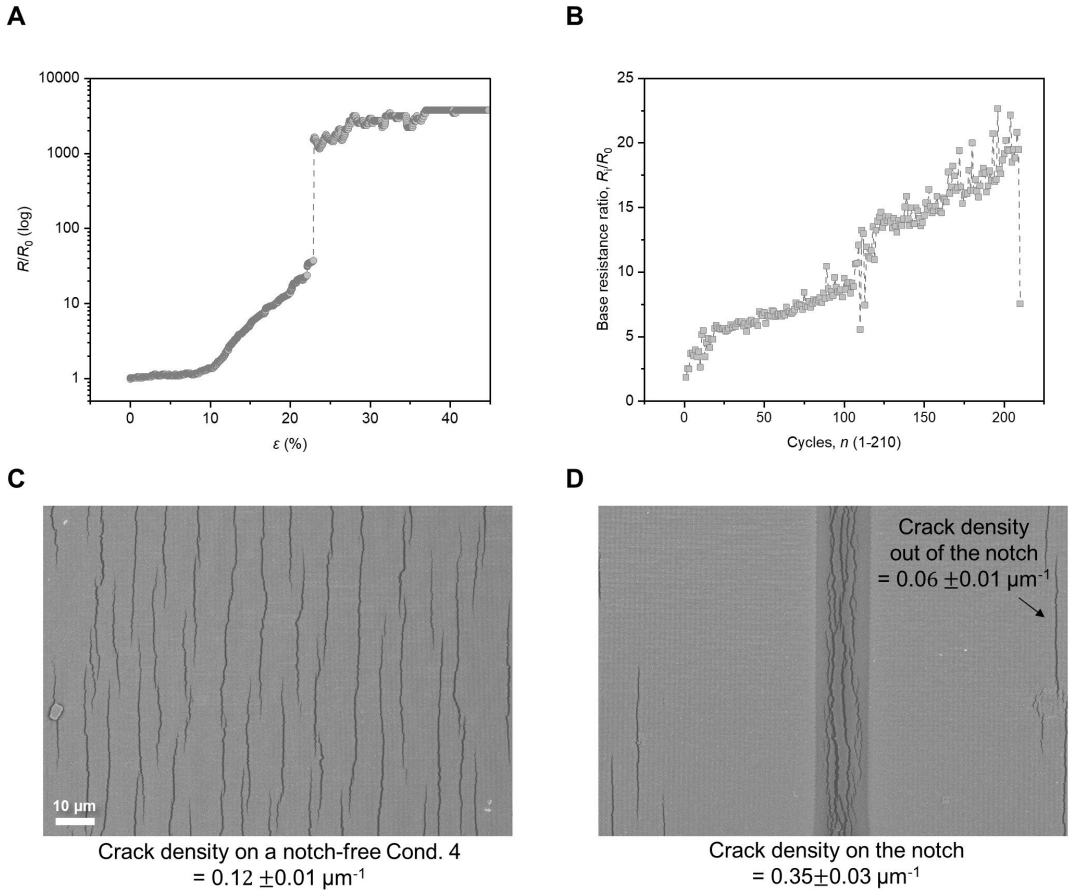

Supplementary Figure 9. Tensile responses of a Cond. 4 specimen fabricated on a flat substrate without a U-shaped notch (NOA + plasma-induced nanostructures + HMDSO + Pt). (A) R/R_0 vs. ε response under monotonic tensile loading (Y-axis: log scale). The resistance increases gradually in the initial strain regime and then rises sharply near ε≈20%, approaching a near-off-state saturation response, which is qualitatively distinct from the continuous percolation-type resistance increase observed in Cond. 1. The dashed line indicates the strain region of abrupt resistance transition.; (B) Cycle-by-cycle baseline resistance ratio (R/R_0) recorded over 210 repeated tensile cycles. Although a partially reversible switching response is observed, the baseline exhibits a continuous upward drift with increasing cycle number, in clear contrast to the stable baseline response of Cond. 4 with a U-shaped notch (Fig. 5A). (C) SEM image of the notch-free Cond. 4 specimen under tensile loading. Cracks form across the active area without a predefined localization site, yielding a uniform crack density of 0.12 ± 0.01 μm^{-1}. Scale bar: 10 μm. (D) SEM image of the notched Cond. 4 specimen under identical tensile loading. Cracks are strongly localized within and immediately adjacent to the U-shaped notch channel, with a crack density of 0.35 ± 0.03 μm^{-1} on the notch, while the region outside the notch retains a substantially lower density of 0.06 ± 0.01 μm^{-1}. These results suggest that the notch plays a role as a geometric stress concentrator that spatially localizes crack initiation sites and improves cycle-to-cycle stability.

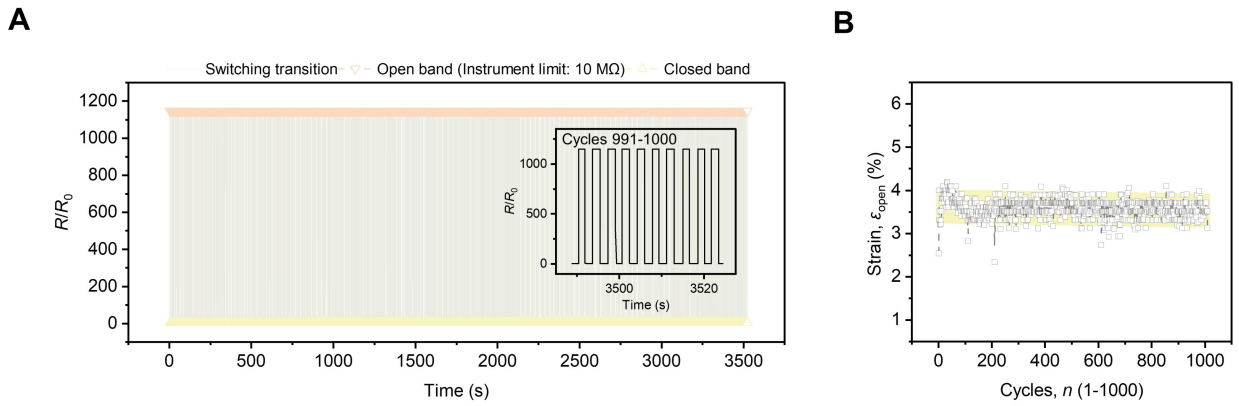

Supplementary Figure 10. Long-term cyclic reliability of a representative Cond. 4 device over 1000 cycles. (A) R/R_0 response as a function of time. The closed band (yellow), switching transition region (salmon), and open band (instrument upper limit: 10 MΩ, orange) are indicated by shaded regions. Over 1000 cycles, the binary-like on/off switching function is maintained without catastrophic failure, although a finite closed-state baseline drift remains, with the closed-state R/R_0 gradually increasing from 0.93 at cycle 1 to 3.17 at cycle 1000. Importantly, the switching contrast is nonetheless preserved: during cycles 991–1000, the open-state R/R_0 after crack opening reached approximately 1.15×10^3 (instrument upper limit, ~10 MΩ), while the closed-state R/R_0 remained at 3.26 ± 0.05, retaining an off-/closed-state resistance separation of approximately 3.5×10^2 and a distinguishable binary readout despite the residual baseline drift. Inset: representative R/R_0 vs. time loops for cycles 991–1000. (B) Cycle-by-cycle switching strain ε_{open} over 1000 cycles. Following the initial conditioning period, ε_{open} stabilizes at an average of $3.58 \pm 0.20\%$ (range: 2.33–4.18%, yellow band), supporting the proof-of-concept-level reproducibility of the crack-opening threshold even under extended cyclic conditions.